**Correspondence to:**
K. Takahashi,
kazue.takahashi@jhuapl.edu

# Polarization of Magnetospheric ULF Waves Excited by an Interplanetary Shock on 27 February 2014

**Kazue Takahashi[1]** , **Tom Elsden[2]** , **Andrew N. Wright[2]** , and **Alexander W. Degeling[3]**

[1]The Johns Hopkins University Applied Physics Laboratory, Laurel, MD, USA, [2]Department of Mathematics and Statistics, University of St Andrews, St Andrews, UK, [3]Shandong Key Laboratory of Optical Astronomy and Solar-Terrestrial Environment, School of Space Science and Physics, Institute of Space Sciences, Shandong University, Weihai, People's Republic of China

**Abstract** Many previous studies have reported that magnetospheric ultralow frequency waves excited by interplanetary shocks exhibit a strong toroidal component, corresponding to azimuthal displacement of magnetic field lines. However, the toroidal oscillations excited by an interplanetary shock on 27 February 2014 and observed on the dayside by multiple spacecraft were accompanied by a strong poloidal component (radial field line displacement). The frequency of the toroidal oscillations changed with the radial distance of the spacecraft as expected for standing Alfvén waves. We run a 3D linear numerical simulation of this wave event using a model magnetosphere with a realistic radial variation of the Alfvén velocity. The simulated wave fields, when sampled at a radial distance comparable to those of the observations in the real magnetosphere, exhibit polarization similar to the observations. In the simulation, the poloidal component comes from radially standing fast mode waves and the toroidal component results from a field line resonance driven by the fast mode waves. As a consequence, the relative amplitude and phase of the toroidal and poloidal components change with radial distance.

**Plain Language Summary** The magnetosphere is strongly disturbed when an interplanetary shock arrives. The disturbance suddenly displaces magnetospheric plasma from its initial position, and as the shock moves away, the displacement is reduced by the tension and pressure of the geomagnetic field. This compression by the passing shock front launches global compressional waves in the dayside magnetosphere, resulting in field line oscillations primarily in the radial direction. Inhomogeneity within the magnetosphere causes these waves to refract away from the radial direction, introducing an azimuthal component to the field line oscillations, and allowing the resonant transfer of energy to natural standing modes of vibration (primarily in the azimuthal direction) of individual field lines (a process known as field line resonance). In this way, the azimuthal and radial oscillations are coupled, but their relative strength depends on location. This paper presents an example of particularly strong radial oscillations using spacecraft data and numerical simulation.

## 1. Introduction

Magnetospheric magnetohydrodynamic (MHD) standing Alfvén waves are often classified into toroidal and poloidal modes. In an axisymmetric magnetosphere, with the coordinate axes as defined in Figure 1a, the idealized toroidal waves (Radoski & Carovillano, 1966) produce perturbations in the azimuthal component of the magnetic field ($\delta B_\phi$), the azimuthal component of the plasma bulk velocity ($\delta V_\phi$), and the radial component of the electric field ($\delta E_\nu$), whereas the idealized poloidal waves (Radoski, 1967) produce perturbations in the radial component of the magnetic field ($\delta B_\nu$), the radial component of the velocity ($\delta V_\nu$), and the azimuthal component of the electric field ($\delta E_\phi$). In the real magnetosphere, the two modes are coupled because of the radial inhomogeneity of the magnetospheric plasma and the finite scale size of the source disturbances that excite the waves. The coupling is mediated by fast mode waves, as described by the theory of field line resonance (FLR) (Chen & Hasegawa, 1974; Southwood, 1974). According to the theory, the excited Alfvén waves exhibit a strong toroidal component, as has been confirmed by spacecraft observations (Arthur & McPherron, 1981; Junginger et al., 1984; Takahashi et al., 2015).

The relative strength of the toroidal and poloidal components is important when one considers the effect of ultralow frequency (ULF) waves on charged particles. In the ring current and radiation belts, the zeroth-order drift velocity ($\mathbf{V}_d$) of energetic particles is dominated by the azimuthal component $V_\phi$. Therefore, $\delta E_\phi$ associated with

**Validation:** Kazue Takahashi, Tom Elsden

**Visualization:** Kazue Takahashi, Tom Elsden

**Writing – original draft:** Kazue Takahashi, Tom Elsden, Andrew N. Wright, Alexander W. Degeling

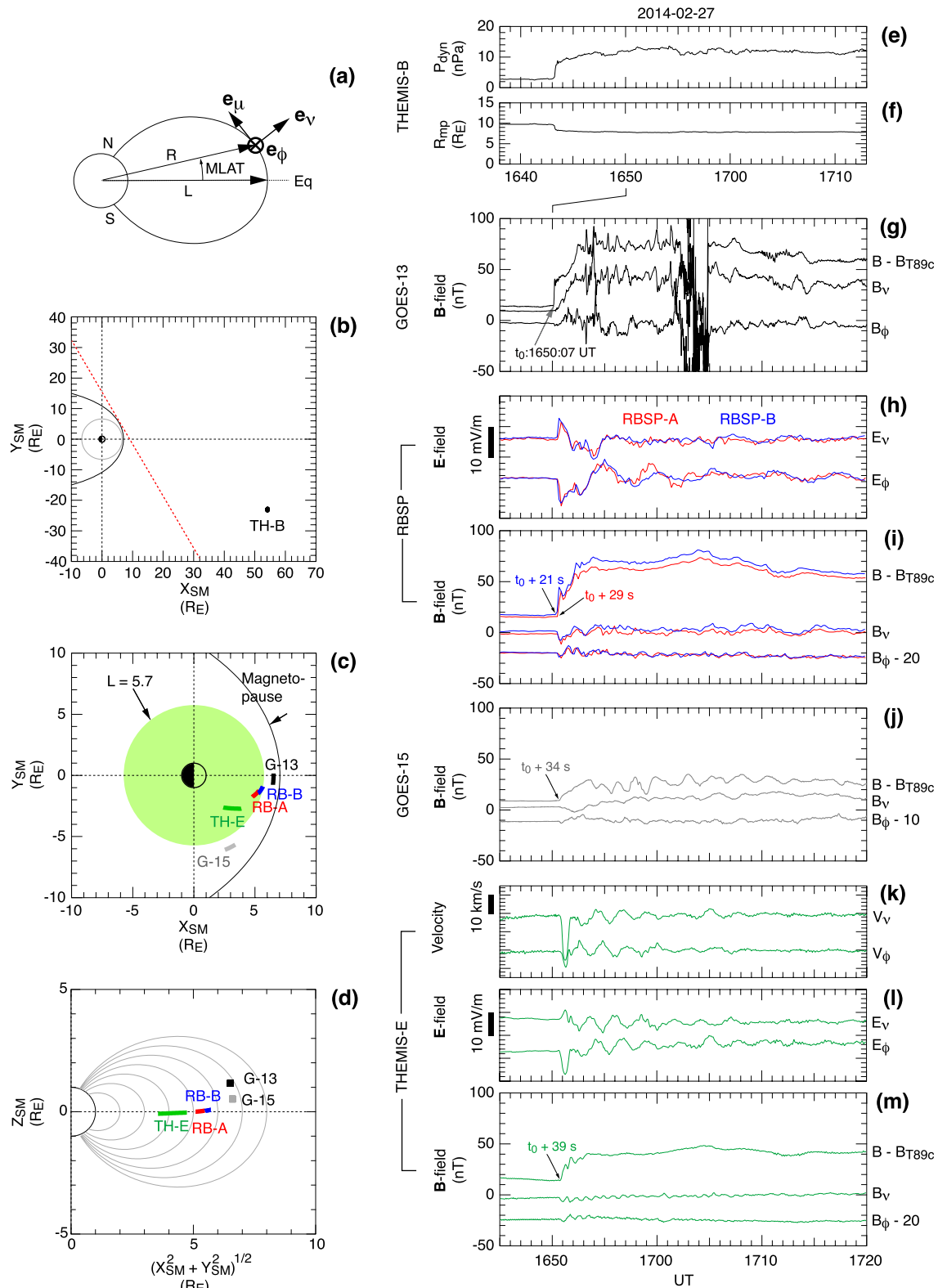**Writing – review & editing:** Kazue Takahashi, Tom Elsden, Andrew N. Wright, Alexander W. Degeling

Figure 1.

poloidal waves is relevant to particle acceleration/deceleration because energy exchange occurs between waves and particles though the $\delta \mathbf{E} \cdot \mathbf{V}_d$ term (Elkington et al., 1999; Ukhorskiy et al., 2005; Wygant et al., 1994). This consideration warrants further investigations of the polarization of magnetospheric ULF waves.

In this study, we examine the polarization of standing Alfvén waves excited by an interplanetary (IP) shock on 27 February 2014 when multiple spacecraft were in the dayside magnetosphere. The waves exhibited a strong poloidal component ($\delta B_\nu \geq \delta B_\phi$) at some locations. In most previous studies of ULF waves excited by an IP shock, the waves were found to be dominated by the toroidal component ($\delta B_\phi \gg \delta B_\nu$) (Baumjohann et al., 1984; Cahill et al., 1990; Kaufmann & Walker, 1974; Kim, 2002; Laakso & Schmidt, 1989; Shi et al., 2013). We discuss possible causes of the poloidal polarization using a numerical simulation.

The remainder of the study is organized as follows. Section 2 describes the experiments and data, Section 3 presents the observations, Section 4 presents the numerical simulation, Section 5 presents the discussion, and Section 6 presents the conclusions.

## 2. Experiments

Data used in this study were obtained using spacecraft experiments and ground magnetometers. The spacecraft data are the vector quantities denoted $\mathbf{E}$ (electric field; Bonnell et al., 2008), $\mathbf{B}$ (magnetic field; Auster et al., 2008), and $\mathbf{V}$ (ion bulk velocity; McFadden et al., 2008) from the Time History of Events and Macroscale Interactions during Substorms (THEMIS) spacecraft; the $\mathbf{E}$-field (Wygant et al., 2013), $\mathbf{B}$-field (Kletzing et al., 2013), and the electron density ($n_e$, derived from plasma wave spectra) (Kurth et al., 2015) from the Van Allen Probes (Radiation Belt Storm Probes, RBSP) A and B spacecraft; and the $\mathbf{B}$-field from the Geostationary Operational Environmental Satellite (GOES)-15 spacecraft (Singer et al., 1996). The ground data are the $\mathbf{B}$-fields measured by the European quasi-Meridional Magnetometer Array (EMMA) network (Lichtenberger et al., 2013).

The 3D $\mathbf{E}$-field vector samples at Van Allen Probes and THEMIS are constructed from the two orthogonal components measured in the spacecraft spin plane and a third component derived using the $\mathbf{E} \cdot \mathbf{B} = 0$ assumption. We express magnetospheric $\mathbf{E}$, $\mathbf{B}$, and $\mathbf{V}$ vectors in the magnetic field-aligned (MFA) coordinate system illustrated in Figure 1a, where the $\mu$ component is defined using a reference background magnetic field ($\mathbf{B}_{ref}$) and the spacecraft position vector ($\mathbf{R}_{sc}$) (Takahashi & Denton, 2021), the $\phi$ (eastward) component is in the direction of $\mathbf{B}_{ref} \times \mathbf{R}_{sc}$, and the $\nu$ (outward) component is in the direction of $\mathbf{e}_\phi \times \mathbf{e}_\mu$. To specify spacecraft positions, we use dipole coordinates $L$ (equatorial distance to the field line passing the spacecraft), MLAT (magnetic latitude), and MLT (magnetic local time).

## 3. Spacecraft Observations

### 3.1. Overview

Figure 1 presents an overview of the multispacecraft observations of shock-induced ULF waves on 27 February 2014. The solar wind was observed by THEMIS-B ~50 $R_E$ upstream of the magnetosphere (Figure 1b). Magnetospheric ULF waves were observed in the prenoon sector by GOES-13, GOES-15, RBSP-A, RBSP-B, and THEMIS-E (Figure 1c). All these spacecrafts were located near the magnetic equator (Figure 1d). The dynamic pressure at THEMIS-B increased at 1643 UT from ~3 to ~10 nPa, signaling the arrival of an IP shock (Figure 1e). The dynamic pressure then slowly increased and reached a maximum value of ~13 nPa. The shock arrived at the magnetosphere ~7 min later. According to the Shue et al. (1998) model, the shock changed the magnetopause standoff distance from ~10 to ~8 $R_E$ (Figure 1f). Figures 1b and 1c include the postcompression magnetopause given by the model. We note that the same shock event was studied by Korotova et al. (2018), who

**Figure 1.** Overview of spacecraft observations at 1645–1720 UT on 27 February 2014. (a) Parameters to specify satellite position in dipole coordinates and the axes of locally defined magnetic field-aligned (MFA) coordinates. (b) Location of THEMIS-B projected to the equatorial plane of solar magnetic (SM) coordinates. The red dashed line indicates the inferred orientation of the shock front. (c) Same as (b) but for the spacecraft located in the magnetosphere. The magnetopause is scaled to the postshock standoff distance shown in panel (f). The green shaded region is an axisymmetric plasmasphere with the outer edge (plasmapause) set at $L = 5.7$ based on the data shown in Figure 4. (d) Location of the spacecraft on the dipole meridian plane of the spacecraft. (e) Solar wind dynamic pressure measured by THEMIS-B. The time is shifted by 7 min relative to magnetospheric time series to account for the delay time to the magnetopause. (f) Magnetopause standoff distance according to Shue et al. (1998) obtained using THEMIS-B data as input. (g) Magnetic field at GOES-13. The components are radial ($B_\nu$), azimuthal ($B_\phi$), and compressional ($B - B_{T89c}$), defined using the T89c model magnetic field as the reference. (h, i) $\mathbf{E}$-field and $\mathbf{B}$-field at RBSP-A. (j) $\mathbf{B}$-field at GOES-15. (k, l, m) Ion bulk velocity, $\mathbf{E}$-field and $\mathbf{B}$-field at THEMIS-E.

**Table 1**
*Shock Impact Arrival Times*

| Spacecraft | Arrival UT (hhmm:ss) | Delay (s) | $L$ | MLAT (°) | MLT (h) |
|---|---|---|---|---|---|
| GOES-13 | 1650:07 | – | 6.83 | 10.13 | 11.80 |
| RBSP-B | 1650:28 | 21 | 5.52 | 0.45 | 11.04 |
| RBSP-A | 1650:36 | 29 | 5.16 | 0.07 | 10.73 |
| GOES-15 | 1650:41 | 34 | 6.66 | 4.51 | 7.61 |
| THEMIS-E | 1650:46 | 39 | 3.77 | −1.11 | 9.01 |

highlighted the relationship between magnetospheric ULF waves and particle flux variations.

Recognizing that the orientation of the shock plane is a major factor affecting the magnetospheric response to IP shocks (Oliveira et al., 2020), we estimated the direction of the shock normal. We used four of the methods reviewed by Oliveira and Samsonov (2018) to determine the normal at THEMIS-B. The normal vectors, called $\mathbf{n}_{MD1}$, $\mathbf{n}_{MD2}$, $\mathbf{n}_{MD3}$, and $\mathbf{n}_{VC}$, were obtained by using the magnetic field and bulk velocity vectors measured by THEMIS-B and averaged in a 10-s data window starting at 1643:00 UT (upstream region) and at 1643:30 UT (downstream region). The four normal vectors are all very similar, with their $x$-$y$-$z$ components given as (−0.87, −0.47, −0.15) in geocentric solar ecliptic coordinates and (−0.86, −0.38, −0.34) in solar magnetic (SM) coordinates. The errors associated with the four methods are small (<4°) for the particular shock event, according to the results obtained using data from the WIND spacecraft and included in the Center for Astrophysics Interplanetary Shock Database (https://lweb.cfa.harvard.edu/shocks). The normal makes an angle of 30° with the Sun-Earth line in such a way that the initial magnetospheric impact by the shock occurs in the postnoon sector as illustrated in Figure 1b and in the northern part of the magnetosphere substantially away from the dipole equator. With this geometry, we expect the magnetospheric distortion caused by the impact to be asymmetric about the magnetic equator and the resulting standing Alfvén waves to consist of both symmetric (even) and antisymmetric (odd) modes.

An obvious consequence of the initial shock contact in the postnoon sector is that the MLT center (denoted $MLT_{impact}$) of fast mode waves is located in the postnoon sector. Using the concept of waveguide modes (e.g., Wright, 1994) with their longitudinal structure specified by the azimuthal wave number $m$, we envision $m = 0$ at $MLT = MLT_{impact}$, $m > 0$ (eastward propagation) at $MLT > MLT_{impact}$, and $m < 0$ (westward propagation) at $MLT < MLT_{impact}$, analogous to a model for Pi2 pulsations (Takahashi et al., 1995). In terms of polarization, the waves will be purely poloidal at $MLT = MLT_{impact}$ but will acquire a toroidal component elsewhere.

Figures 1g–1m show data from the magnetospheric spacecraft for 1645–1720 UT. According to the schematic axisymmetric plasmasphere with a radius of $L = 5.7$ (Figure 1c) corresponding to the plasmapause inner edge encountered by RBSP and THEMIS-E (see Figure 4), THEMIS-E was well inside the plasmasphere, RBSP-A and RBSP-B were in the plasmasphere but close to the plasmapause, GOES-13 was probably outside the plasmasphere (no $n_e$ data are available from this spacecraft) and very close to the magnetopause, and GOES-15 was in the plasmatrough. The vector variables in these figures are presented in the MFA coordinate system in which $\mathbf{B}_{ref}$ is given by the T89c model (Tsyganenko, 1989). $B_{T89c}$ denotes the magnitude of the model field. Because the only input to the T89c model is the Kp index, which is constant over a 3-hr interval, the model does not produce sudden changes arising from the IP shock.

At each spacecraft, a sudden magnetic field compression is evident after ~1650 UT. Table 1 lists the start time of the compression and the location of observation for each spacecraft. The start time is determined by visually examining the $B − B_{T89c}$ time series plotted at a time resolution of 1 s or higher, and the spacecraft locations are defined using a centered dipole based on the Gauss coefficients of the International Geomagnetic Reference Field (IGRF) model (Alken et al., 2021). GOES-13, located closest to the magnetopause, was the first to detect the compression, at 1650:07 UT. The detection times are also included in Figures 1i (RBSP-A and RBSP-B), 1j (GOES-15), and 1m (THEMIS-E). The maximum delay of 39 s occurred at THEMIS-E, indicating the compression propagated tailward as expected. An apparent tailward propagation velocity is found to be 710 km/s by dividing the distance (3.8 $R_E$) between GOES-13 and THEMIS-E along the Sun-Earth line by the delay time.

### 3.2. Oscillations Observed After the Compression

Figure 1 shows that the sudden magnetic compression was followed by position-dependent magnetospheric oscillations, including both transverse and compressional types. Table 2 summarizes the oscillations. Assuming that the transverse oscillations resulted from standing Alfvén waves, we assign harmonic mode numbers to them. They are either 1 (fundamental) or 2 (second harmonic).

GOES-13, which was located at $L = 6.83$ and closest to the postcompression magnetopause, detected large-amplitude (~20 nT peak-to-peak) quasiperiodic (~1 min) oscillations in the $B_\nu$ and $B_\phi$ components at

**Table 2**
*Oscillations Observed After the Shock Impact*

| Spacecraft | Component | UT | $L$ | Period (s) | Frequency (mHz) | Harmonic mode |
|---|---|---|---|---|---|---|
| RBSP-B | $E_\phi$ | 1655–1717 | 5.56–5.70 | 334 | 3.0 | 1 |
| THEMIS-E | $V_\nu$ | 1654–1707 | 3.88–4.32 | 156 | 6.4 | 1 |
| THEMIS-E | $V_\phi$ | 1652–1708 | 3.81–4.35 | 158 | 6.3 | 1 |
| THEMIS-E | $E_\nu$ | 1653–1707 | 3.84–4.32 | 160 | 6.3 | 1 |
| THEMIS-E | $E_\phi$ | 1654–1707 | 3.88–4.32 | 161 | 6.2 | 1 |
| THEMIS-E | $B_\nu$ | 1651–1657 | 3.78–3.99 | 53.7 | 18.6 | 2 |
| THEMIS-E | $B_\phi$ | 1651–1654 | 3.78–3.88 | 53.7 | 18.6 | 2 |
| THEMIS-E | $B$ | 1651–1653 | 3.78–3.85 | 45.1 | 22.2 | – |
| GOES-15 | $B$ | 1703–1710 | 6.66 | 151 | 6.6 | – |

1652–1702 UT before briefly entering the magnetosheath. The oscillations are similar to 50-s oscillations in the low-latitude boundary layer detected by the Spacecraft Charging at High Altitudes spacecraft during a major magnetospheric compression event (Takahashi et al., 1991). After reentering the magnetosphere at ~1705 UT, GOES-13 detected irregular oscillations with lower amplitudes.

RBSP-A and RBSP-B were moving outward at smaller geocentric distances (5.09–5.71 $R_E$) with a radial separation of 0.2–0.4 $R_E$. The two spacecraft detected very similar oscillations as expected, with $E_\phi$ exhibiting a period of 330 s. The **B**-field variations are irregular overall and lack the 330 s periodicity, and they also differ from the 1-min **B**-field oscillations detected by GOES-13.

GOES-15 was moving sunward near dawn. At this spacecraft, magnetic field oscillations are most prominent in the $B$ component. The oscillations start ~3 min after the compression and exhibit a period of ~90 s for a few cycles. Then, after ~1700 UT, the period increases to ~150 s. We attribute these oscillations to either cavity mode resonances or an internal instability because they do not match the $P_{dyn}$ variations shown in Figure 1e.

THEMIS-E was also moving sunward from $L = 3.6$ to $L = 4.7$ very near the magnetic equator. Both **V** and **E** at this spacecraft exhibit regular ~2-min oscillations with comparable amplitudes in the $\nu$ and $\phi$ components. The **B**-field exhibits periodic oscillations in all components. The $B$ oscillation has a period of ~40 s and lasts only a few cycles. The $B_\nu$ oscillations have a period of ~50 s and last ~20 min. The $B_\phi$ oscillation is similar to the $B_\nu$ oscillation but diminishes in ~5 min. The relative duration of the $B_\nu$ and $B_\phi$ oscillations is opposite to what is expected for the typical poloidal-toroidal mode coupling (Mann & Wright, 1995). We attribute the $B_\nu$ and $B_\phi$ oscillations to second harmonic standing Alfvén waves because the observation was made at the equator where the fundamental waves have a node of the $B_\nu$ and $B_\phi$ components.

### 3.3. Frequency of Standing Alfvén Waves

We examine the spatial variation of standing Alfvén wave frequencies because it can affect the polarization of shock-induced ULF waves. Here, we use data from RBSP-A, THEMIS-E, and EMMA.

Figure 2 shows the RBSP-A data. In the $E_\nu$ spectra (Figure 2a), spectral lines labeled $f_1$ and $f_3$ are evident before the shock impact. These correspond to the fundamental and third harmonics of standing Alfvén waves. The second harmonic ($f_2$) is missing because the spacecraft was located at the equator, which is the expected location of an $E_\nu$ node of the harmonic. Spectral lines become somewhat obscure after the shock impact due in part to a strong modulation of the wave amplitude, which causes some pixels to become nearly saturated. The $B_\phi$ spectra (Figure 2b) exhibit only the $f_2$ line because the fundamental and third harmonics have a $B_\phi$ node at the equator. Figure 2c shows the $E_\nu/B_\phi$ power ratio to help frequency identification by suppressing the effect of amplitude modulations. For harmonic modes having a $B_\phi$ node near the spacecraft, the ratio becomes high and produces dark pixels. The inverse (light pixels) occurs for harmonic modes having an $E_\nu$ node near the spacecraft. Figure 2c shows $f_2$ and $f_3$ signatures at 1730–1800 UT. We judge that the spacecraft was within the plasmasphere because $n_e$ (Figure 2d) maintains values higher than 47 cm$^{-3}$, which is higher than the typical plasmatrough values (<10 cm$^{-3}$), and shows no sign of a sharp decrease.

Figure 1 shows the THEMIS-E data. The preshock portion of the dynamic spectra (Figures 3a–3c) shows a steadily falling $f_1$ line. The postshock portion of the spectra exhibits signatures of the $f_1, f_2,$ and $f_3$ oscillations. There is
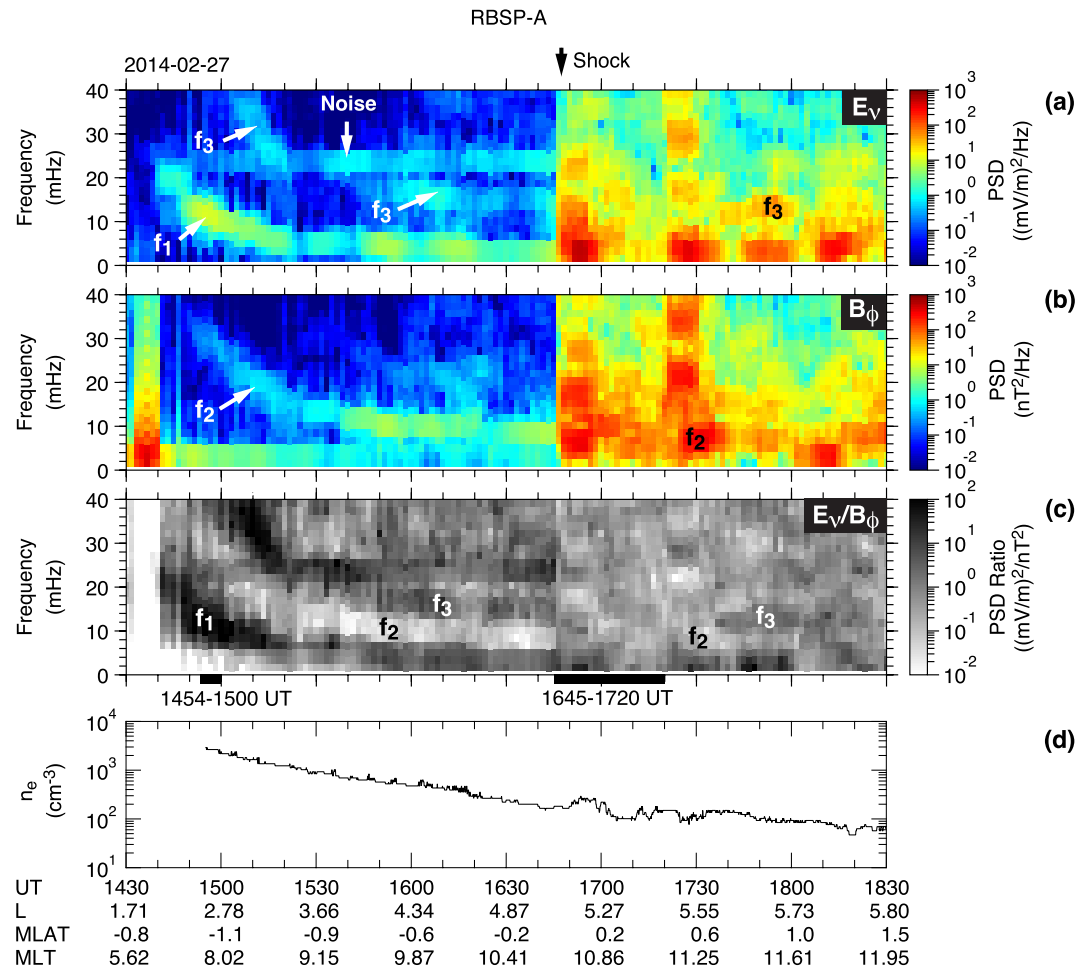
**Figure 2.** Wave frequencies at RBSP-A. (a) Dynamic spectra of the $E_\nu$ component. The fundamental ($f_1$) and third harmonic ($f_3$) frequencies are labeled. The steady spectral peak at 25 mHz is an artifact. The arrowhead at the top marks the arrival of the shock. (b) Dynamic spectra of the $B_\phi$ component. (c) $E_\nu$ to $B_\phi$ power spectral density (PSD) ratio. The horizontal black bars at the bottom inidcate the time intervals covered by Figure 1 (1645–1720 UT) and Figure 5 (1454–1500 UT). (d) Electron density indicating that the spacecraft was in the plasmasphere.

no obvious change in $f_1$ across the shock compression, implying that the mass density changed little. The shock increased the **B**-field magnitude at THEMIS-E by ∼30 nT, but this change is only ∼5% of the total magnitude and cannot contribute to a large change in Alfvén wave frequencies. An abrupt increase in these frequencies does occur at ∼1740 UT in association with the spacecraft exit from the plasmasphere (Figure 3d).

Figure 4 illustrates the $L$ dependence of the $f_1$ values derived from the spectral data shown in Figures 2 and 3. The figure includes the $f_1$ values derived using data from 24 EMMA stations available for the selected day. We used the standard cross-phase technique (Waters et al., 1991) to determine $f_1$ at EMMA. The panels on the left show the measurement locations projected onto the SM equatorial plane using either the IGRF model (Figure 4a) or the centered dipole (Figures 4c and 4f). The panels on the right show the $L$ profiles of $f_1$ determined at EMMA, RBSP-A, and THEMIS-E. The EMMA results were obtained for a preshock epoch of 1200 UT. The RBSP-A results were obtained for 1455–1830 UT from the $f_1$, $f_2$, and $f_3$ spectral lines visible in Figure 2. In addition to the genuine $f_1$ values, we include $f_1$ values estimated using the relationship $f_1 = 0.40f_2$ or $f_1 = 0.25f_3$ known from a statistical study of toroidal wave frequencies at RBSP (Takahashi & Denton, 2021). The THEMIS-E results were similarly obtained for 1615–1830 UT from the $f_1$, $f_2$, and $f_3$ spectral lines visible in Figure 3.

The $f_1$ values at RBSP-A and THEMIS-E decrease with $L$ from deep inside the plasmasphere ($L < 3$) to $L = 5.6$ (RBSP-A) or $L = 5.4$ (THEMIS-E), which roughly correspond to the inner edge of the plasmapause (vertical dashed lines in Figures 4d, 4e, 4g, and 4h) identified from the $n_e$ data (RBSP-A) or spacecraft potential data
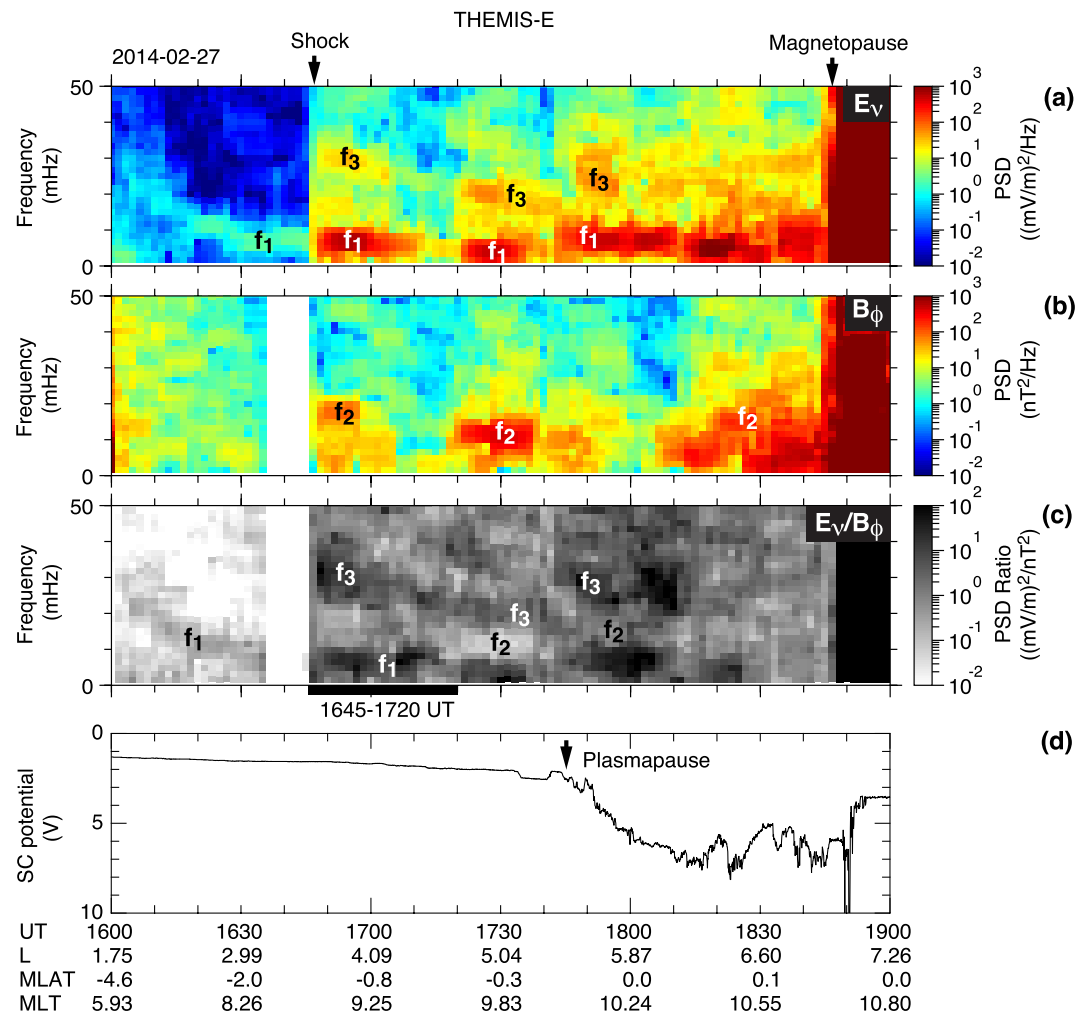
**Figure 3.** Wave frequencies at THEMIS-E. (a) Dynamic spectra of the $E_\nu$ component. The fundamental ($f_1$) and third harmonic ($f_3$) frequencies are labeled. The arrowhead at the top marks the arrival of the shock. (b) Dynamic spectra of the $B_\phi$ component. (c) $E_\nu$ to $B_\phi$ power spectral density (PSD) ratio. The horizontal black bar inicates the time interval covered by Figure 1. (d) Spacecraft (SC) potential. The plasmapause inner edge was encountered at ∼1745 UT.

(THEMIS-E). The plasmapause location is unclear in the EMMA plots, although the last $f_1$ data point ($L \sim 6.8$) shows a slightly higher value than at $L \sim 6.0$, implying an inward mass density gradient. We estimate the plasmapause inner edge to be located at $L \sim 6.4$ (vertical dashed line in Figure 4b). The larger plasmapause distance at EMMA (MLT $\sim$ 1400) implies a plasma bulge or a drainage plume in the postnoon sector. However, we cannot determine the plasmasphere shape on the afternoon side for the time interval of the RBSP-A and THEMIS-E observations.

### 3.4. Polarization of Transverse Oscillations

To emphasize the unique polarization of the shock-driven ULF waves, we first show the polarization of ULF waves observed before the shock impact. Figure 5 shows time series plots and hodograms of perturbations transverse to the background magnetic field detected in the plasmasphere by RBSP-A and RBSP-B before the arrival of the shock. The spacecraft locations are shown in Figures 5a and 5b. The region shaded green in these figures is a schematic axisymmetric plasmasphere with its outer boundary placed at $L = 5.7$. In the hodogram plots, the orange dotted line indicates the coordinate axis associated with toroidal waves.

We have selected three examples of standing Alfvén waves observed at 1454–1500 UT. These are a second harmonic wave appearing in the **B**-field and a fundamental wave appearing in the **E**-field at RBSP-A, and a second harmonic wave appearing in the **B**-field at RBSP-B. Figure 5c summarizes the $L$ location and frequency
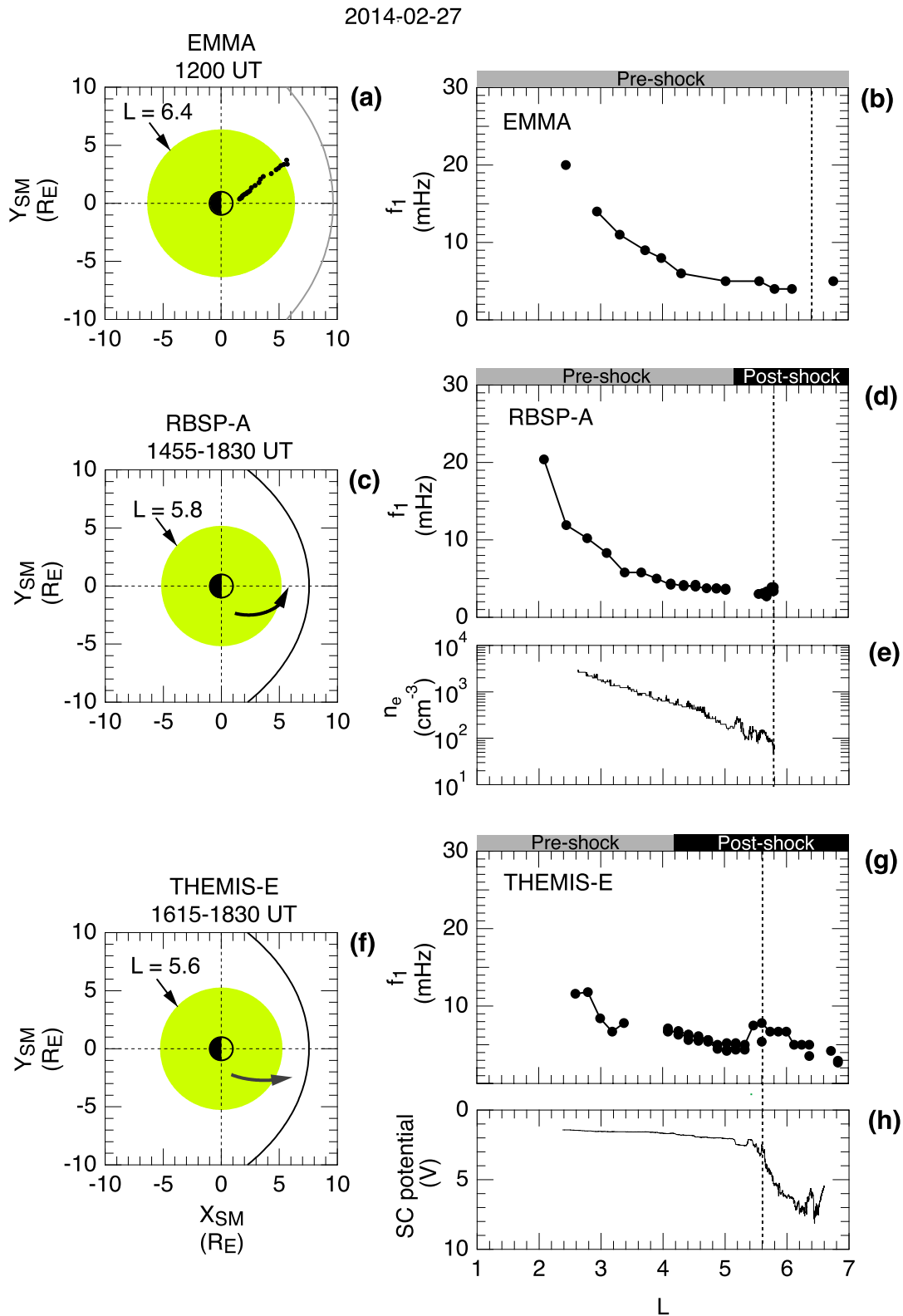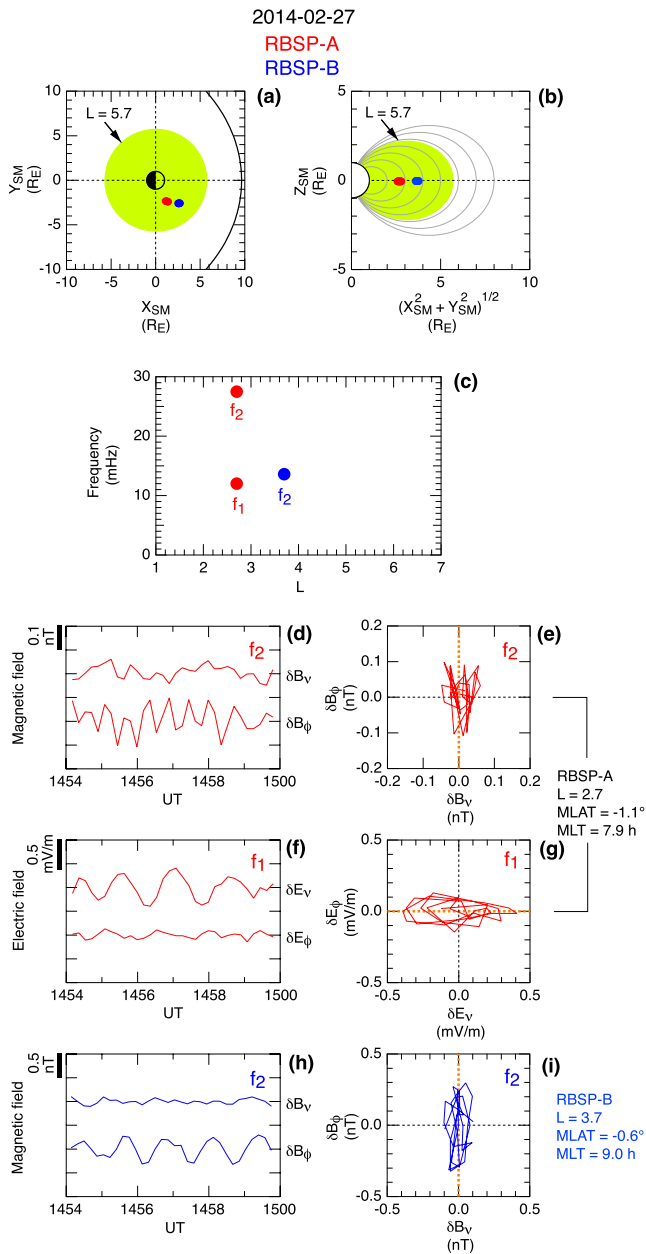
**Figure 4.**

**Figure 5.** Transverse oscillations observed in the plasmasphere before the magnetospheric compression by the interplanetary shock. (a, b) Spacecraft locations in solar magnetic (SM) coordinates. The green shading indicates a model plasmasphere. (c) Frequencies of the three oscillations, shown in the lower panels, plotted versus $L$. The labels indicate the harmonic mode. (d, e) Time series and hodograms of the second harmonic magnetic field oscillation at RBSP-A. The orange dotted line in the hodogram plots indicates the direction for toroidal oscillations. (f, g) Same as (d, e) but for the fundamental electric field oscillation. (h, i) Same as (d, e) but for the second harmonic magnetic field oscillation at RBSP-B.

of these waves. The harmonic modes can be easily determined because both spacecraft were located very close to the magnetic equator, where odd modes have a **B**-field node and even modes have an **E**-field node, as already noted in the dynamic spectra (Figures 2 and 3). All these waves exhibit toroidal perturbations with peak-to-peak amplitudes lower than 1 nT or 1 mV/m. These properties are representative of externally driven standing Alfvén waves observed by RBSP in the dayside plasmasphere.

Figure 6 shows time series plots and hodograms of standing Alfvén waves excited immediately after the shock impact. The selected time intervals are 1652–1658 UT for the fundamental and second harmonic waves at THEMIS-E and 1652–1720 UT for the fundamental wave at RBSP-B. These waves all exhibit a poloidal component comparable to or exceeding the toroidal component. Also, the amplitudes of the waves are much larger than those shown in Figure 5. This is explained by the large fast mode impulse generated by the shock and the short distances of the spacecraft from the magnetopause. In Figure 6f, $\delta V_{\nu}$ leads $\delta V_{\phi}$ by a quarter of the wave period, leading to a circular hodogram with a counterclockwise sense of rotation (Figure 6g). A similar rotation is seen in the $\delta B_{\nu} - \delta B_{\phi}$ hodogram (Figure 6e).

Poloidal standing Alfvén waves are routinely excited in the magnetosphere, and they are usually attributed to instabilities driven by ring current ions (Southwood, 1976). However, it is unlikely that the shock-induced standing Alfvén waves with a strong poloidal component are related to ring current instabilities. For example, if we take the fundamental waves detected by RBSP-A and RBSP-B at 1652–1720 UT, there is hardly any phase delay between the two spacecraft (Figure 1g). Internally excited fundamental poloidal waves have an azimuthal wave number ($m$) much larger than 10 (Takahashi et al., 2018) and would produce a large phase delay between the spacecraft, which had an MLT separation of ∼0.3 hr.

## 4. Numerical Simulation

To further investigate the nature of the observed signals, we perform numerical MHD simulations using the model of Wright and Elsden (2020), which will be briefly described here. The code solves the linear MHD equations with the assumption of a cold plasma, in a background dipole magnetic field geometry. Field-aligned coordinates are used to aid numerical efficiency, as well as to provide a natural system in which to study MHD wave phenomena. Figure 7 shows a meridional slice of the simulation domain. The inner and outer boundaries are defined by dipole field lines. The upper and lower (ionospheric) boundaries are curved surfaces in real space, corresponding to a constant value of the field-aligned coordinate $\gamma$ that we use in the simulation. The boundary conditions at the northern/southern ionospheres are taken to be perfectly reflecting (node of velocity/electric field, antinode of magnetic field). The outer boundary of the simulation is defined by the magnetopause location in the equatorial plane set from the approximation of Shue et al. (1997). The subsolar point is taken to be at 7.5 $R_E$ to match that determined by the observations (e.g., Figure 1f) after the shock impact. The inner boundary is taken to be perfectly reflecting at $L = 3$. These features of the simulation domain are apparent from Figure 8, showing the equilibrium Alfvén velocity in the equatorial plane. The
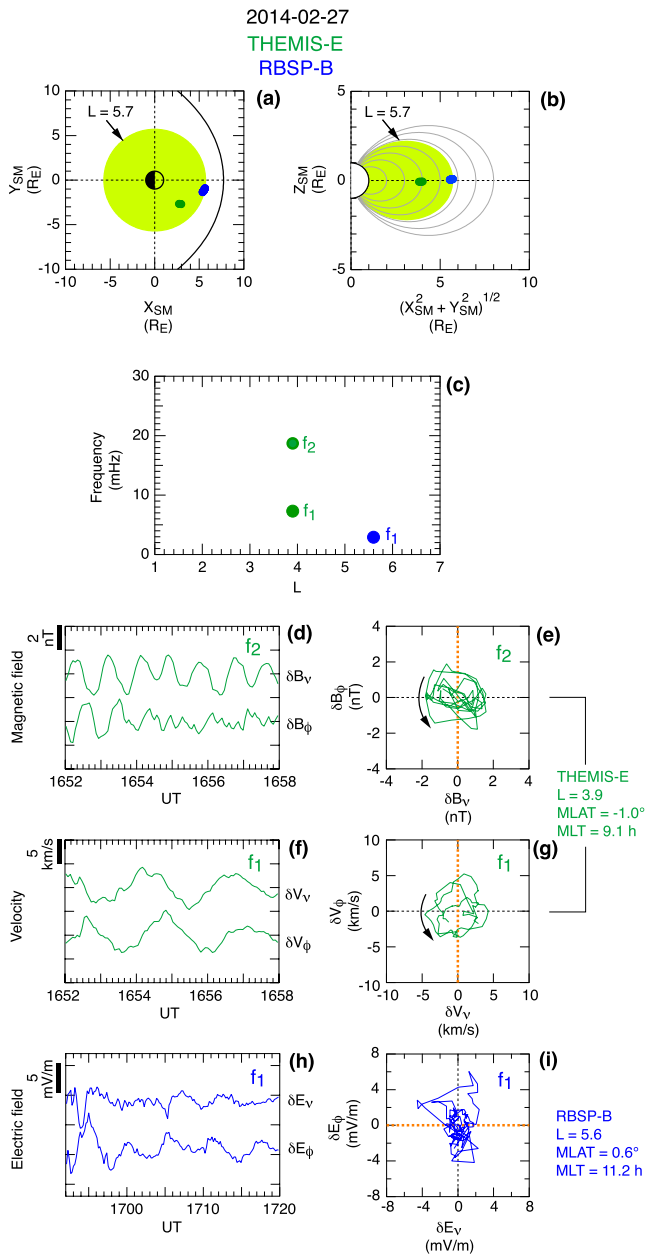
**Figure 4.** (a) Locations of the European quasi-Meridional Magnetometer Array (EMMA) stations at 1200 UT on 27 February 2014 mapped to the equatorial plane of solar magnetic (SM) coordinates along the International Geomagnetic Reference Field (IGRF) model magnetic field lines. (b) $L$ profile of $f_1$ determined using the EMMA data. The vertical dashed line indicates the inferred plasmapause. (c) Location of RBSP-A mapped to the SM equatorial plane along the dipole field lines. (d) $L$ profile of $f_1$ determined using the RBSP-A data. (e) Electron density at RBSP-A. The vertical dashed line indicates the inferred plasmapause. (f, g) Same as (c, d) except for THEMIS-E. (h) Spacecraft (SC) potential at THEMIS-E.

**Figure 6.** Transverse oscillations observed in the plasmasphere immediately after the magnetospheric compression by the interplanetary shock. (a, b) Spacecraft locations in solar magnetic (SM) coordinates. The green shading indicates the inferred plasmasphere. (c) Frequencies of three selected oscillations, shown in the lower panels, plotted versus the $L$ value of observation. The labels indicate the harmonic mode. (d, e) Time series and hodogram of the second harmonic magnetic field oscillation at THEMIS-E. The orange dotted line in the hodogram plots indicates the direction for toroidal oscillations. The black arrow indicates the sense of rotation. (f, g) Same as (d, e) but for the fundamental electric field oscillation. (h, i) Same as (d, e) but for the second harmonic magnetic field oscillation at RBSP-B.

variation of the density along the field (impacting the Alfvén velocity) is chosen to vary proportional to $R^{-4}$, where $R$ is geocentric distance (Figure 1a). Across the field, a radial variation is chosen (see Figure 8b) to approximately model the frequencies observed (e.g., Figure 4), including a sharp change over $L = 5$–6 modeling the plasmapause location, again inferred from the observed data.

The model is driven at the magnetopause boundary through a perturbation to the compressional magnetic field component, to mimic driving by changes to the solar wind dynamic pressure. To model the IP shock impacting the magnetopause, the compressional field component is varied on the magnetopause according to such a propagating front in the solar wind, with a shock normal angle of 30° to the Earth-Sun line in the equatorial plane, and an angle of ~33° to the magnetic equator in a meridian plane, as found from the observations. The driver is a constant amplitude planar front that can be pictured as propagating toward the magnetopause from outside the domain. The amplitude of the perturbation on the magnetopause is determined by resolving the dot product of the magnetopause normal at a given location with the front propagation direction. Because the model is focused on the dayside (see Figure 8a), the driver is switched off far around the flanks, where dissipation regions mimic loss to the tail beyond $X = -6$ $R_E$. Antisunward propagation of the driver around the flanks is modeled through the tailward component of the planar front. The driver is a step (modeled by a hyperbolic tangent function of distance), which is then maintained throughout the simulation duration to model an increased pressure, as seen in the observations. Figure 9 is a plot of the compressional magnetic field just inside the magnetopause boundary at $(X, Y) = (6.26, 4.83\ R_E)$, which is essentially the driver. The compressional magnetic field in the equatorial plane 30 s after the start of the simulation is displayed in Figure 10. The yellow dot marks the location where the time series is taken for Figure 9.

The pressure impulse drives a plethora of wave activity in the simulation. A key aspect for comparison is the observations from the THEMIS-E satellite shown in Figure 6f, where coherent oscillations are observed in both the radial and azimuthal velocity components. Figure 11 displays contours of the radial (panel (a)) and azimuthal (panel (b)) velocity in the equatorial plane, 5.02 min into the simulation. At the location of the white dot, $(X, Y, Z) = (4.07, 0.42, 0.00\ R_E)$, time series are shown of these velocity components in Figure 12a, with the corresponding hodograms in Figure 12b. The equivalent figures for the perpendicular magnetic field components are shown in Figures 12c and 12d and can be compared to the THEMIS-E magnetometer data in Figures 6d and 6e. Together, these figures may be used to discuss the overall simulation behavior and for comparison with the observations.

The impulse propagates through the domain and produces the initial sharp negative $\delta V_\nu$ signature seen in Figure 12a as well as that in the observations (e.g., Figure 1k). This sets up a radially standing fast wave with a coherent frequency, and it is this frequency that is responsible for the $\delta V_\nu$ time series (red) in Figure 12a. The spatial structure of this fast mode is evident from the radial velocity in Figure 11a. However, this only shows the structure at a single time, and in fact there is a region over which the mode is predominantly standing (~11–15 MLT), but propagating around the flanks outside this MLT range. This behavior of fast normal modes was established by Degeling et al. (2010) (their Figure 2 and paragraph 23) and Elsden and Wright (2019) (their Figure

6). The outer portion of the domain out to the magnetopause is not shown here, because the signal there is of larger amplitude and dominates those in the inner region where we wish to compare to satellite observations. The established fast wave drives a series of FLRs throughout the domain, dependent on the chosen Alfvén velocity
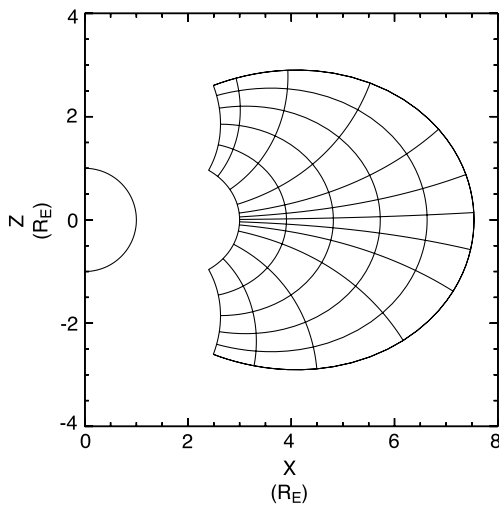
**Figure 7.** Meridional slice of the simulation domain indicating representative magnetic field lines and curves orthogonal to them representing surfaces of constant field-aligned simulation coordinate $\gamma$. The actual grid resolution is much higher.

profile. This is clear in Figure 11b showing $\delta V_\phi$, where narrow toroidal FLRs are clear. The time series in Figure 12 are taken from the inner resonance, better matching the location of the THEMIS-E spacecraft deeper inside the plasmasphere. Considering Figures 12a and 12b, the amplitude of $\delta V_\phi$ (black) initially grows in time, clearly driven by the fast mode, before being damped by the dissipation (resistivity) present in the model. The velocity components are ~90° out of phase (with $\delta V_\nu$ leading), which matches the observations (Figure 6f), and therefore produces an approximately circular hodogram. Figures 12c and 12d provide the same analysis for the perpendicular magnetic field components, which for the given boundary conditions will represent the second field-aligned harmonic. After the initial impulse, these signatures also settle down to being in quadrature, with $\delta B_\nu$ leading $\delta B_\phi$ by ~90° (compare to Figure 6d), again giving circular hodograms. It should be noted that because of the relatively narrow radial structure of the FLR, the signatures are very sensitive to the satellite location. Indeed, across the resonance, there will be a phase change of $\pi$, which would reverse the direction of rotation in the hodograms.

## 5. Discussion

The observations presented here indicate that standing Alfvén waves excited by an IP shock can accompany a substantial poloidal component, a notable departure from the majority of cases reported previously (e.g., Cahill et al., 1990). Our observations were made by multiple spacecraft located in the noon sector, suggesting that poloidal oscillations may not be uncommon when the magnetosphere is disturbed by an IP shock. This section provides
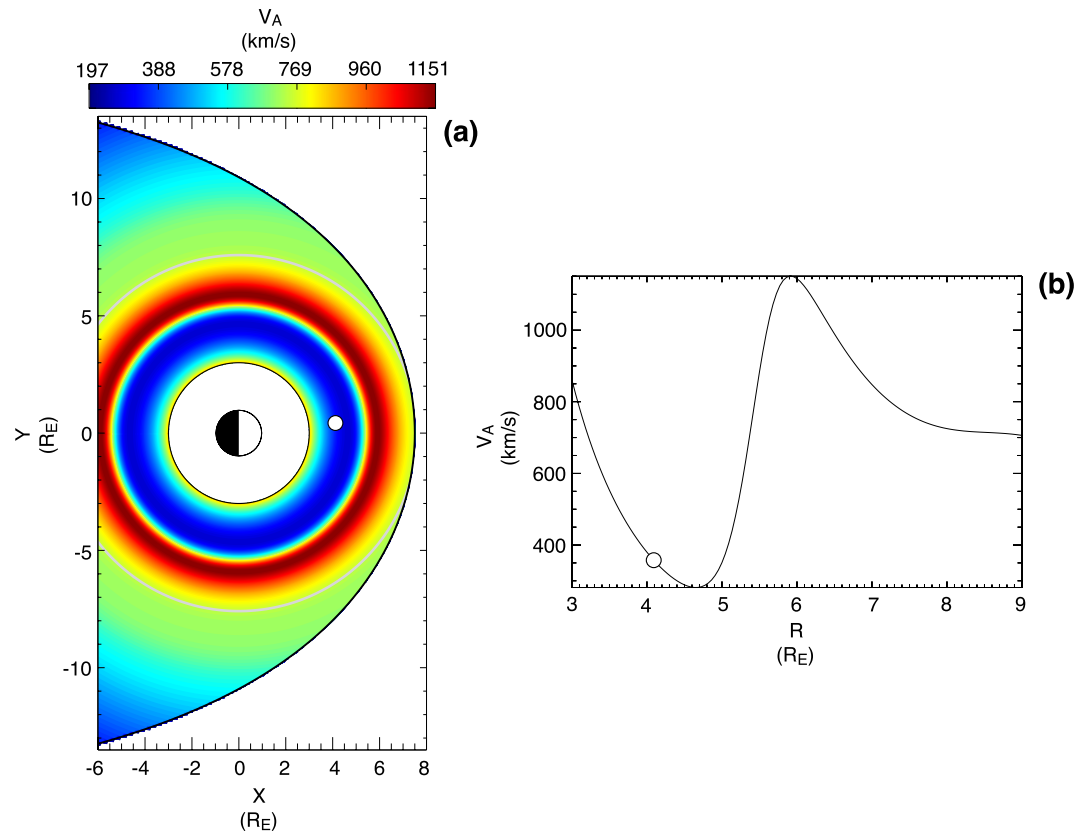


**Figure 8.** (a) Alfvén velocity variation in the equatorial plane. The white dot indicates the location where data are sampled to generate Figure 12. (b) Alfvén velocity variation with radial distance in the equatorial plane. The white dot indicates the location of the white dot in panel (a).
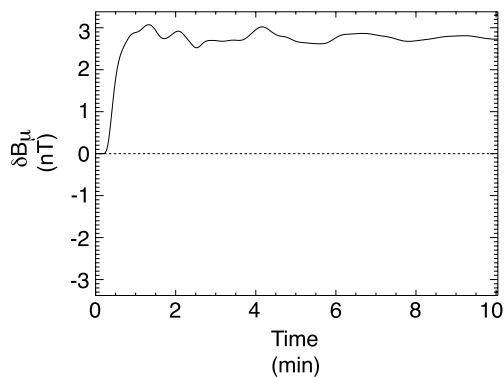
**Figure 9.** Time series of the equatorial magnetic compression at $(X, Y) = (6.26, 4.83\ R_E)$, representing the driver of the simulation.
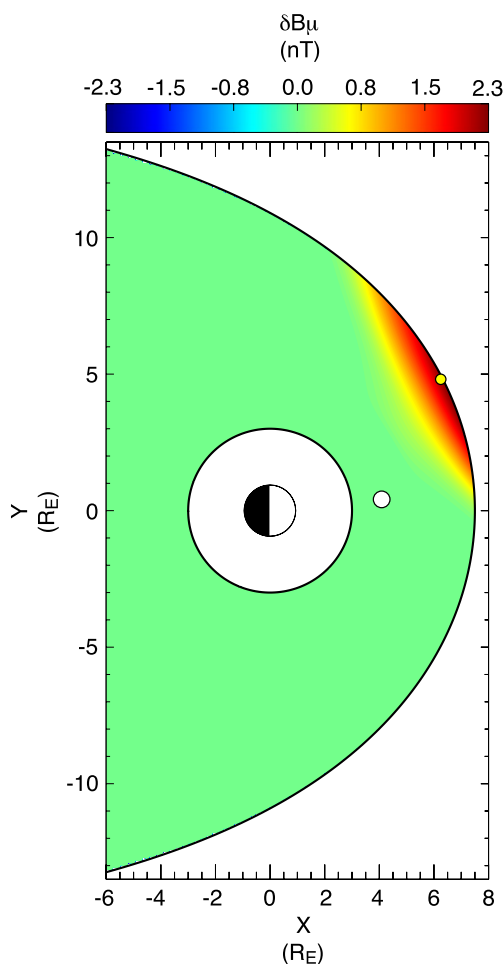


**Figure 10.** The compressional magnetic field perturbation $\delta B_\mu$ in the equatorial plane 30 s after the start of the simulation, indicating the location of the driving impulse. The yellow dot indicates the location where data are sampled to generate Figure 9. The white dot indicates the location where data are sampled to generate Figure 12.

more discussion on the source of the poloidal component and its coupling to FLR.

### 5.1. Coupling of FLR and Fast Mode Waves

In our simulation, the model Alfvén velocity does not have a local time dependence but has a radial structure with a realistic plasmapause gradient. In the simulation, fast mode waves excited by the IP shock establish a radially standing wave or a normal mode, and this global mode excites toroidal standing Alfvén waves through the FLR mechanism. The FLR frequencies change with $L$ while the frequencies of standing fast mode waves do not. When standing fast mode waves are excited at many harmonics, they can couple to standing Alfvén waves on multiple $L$ shells at $L$-dependent frequencies (e.g., Lee & Lysak, 1989), providing an explanation to the $L$ dependence of the frequency of the observed waves (Figure 6c). The amplitude and phase of the toroidal waves change rapidly with distance from the center of FLR, while those of the global mode vary with $L$ differently. As a consequence, the relative amplitude and phase between the poloidal ($\delta V_\nu$, $\delta B_\nu$, and $\delta E_\phi$) and toroidal ($\delta V_\phi$, $\delta B_\phi$, and $\delta E_\nu$) components strongly depend on the location of observation.

Noting that $\delta E_\phi$ and $\delta B_\mu$ of idealized radially standing fast mode waves maintain a phase difference of $\pm 90°$, we examined the phase delay between these field components at THEMIS-E and RBSP-B during the wave events shown in Figure 6. We were unable to obtain a clear signature of the predicted phase delay. This result is not surprising for a dispersive waveguide or a cavity with more than one fast mode present. The presence of multiple azimuthal wave numbers will lead to a complicated phase relation. In addition, a time dependent driving mechanism and energy loss to the nightside magnetosphere will make the $E_\phi - B_\mu$ phase delay time dependent. In a time dependent situation, the fast mode can have a strong propagating component, i.e., as in the initial transient. The $B_\mu$ oscillations tend to decay much more quickly than the FLR fields, so the fast mode likely has a signification propagating component. However, the fast mode could be standing radially while propagating azimuthally.

Obviously, the simulation results should be taken with some caution. For example, the good match between the observation made by THEMIS-E (Figure 6) and the simulation (Figure 12) was obtained when the simulation results were sampled near noon (MLT ~ 12 hr) not at the location of the observation (MLT ~ 9 hr). The reason why the simulation did not accurately reproduce the observation might be the axisymmetric model Alfvén velocity distribution and also the strictly dipolar field line topology, which obviously is very simplistic, and/or a difference of the estimated shock normal orientation from the reality. The shock normal was estimated by using a THEMIS-B observation made ~20 $R_E$ away from the Sun-Earth line (Figure 1b). The shock normal at the point of contact of the shock with the magnetosphere might have been different. In addition, kinetic processes that occur in the foreshock and the magnetosheath could have altered the effective geometry of the shock front (Wang et al., 2019). These geometric considerations are important in understanding the local time variation of the wave fields even when the Alfvén velocity distribution is axisymmetric.

We suggest that shock-induced ULF waves dominated by the toroidal components may be observed in two circumstances. The first is when observations are made near a node of standing fast mode waves. In the case of radially standing fast mode waves, the node of $\delta B_\nu$ and $\delta E_\phi$ is located at different radial distances (Takahashi et al., 2022). Depending on the field vector examined, the poloidal component may not be detected. The second is when the global mode is damped quickly, leaving long-lasting toroidal waves to be
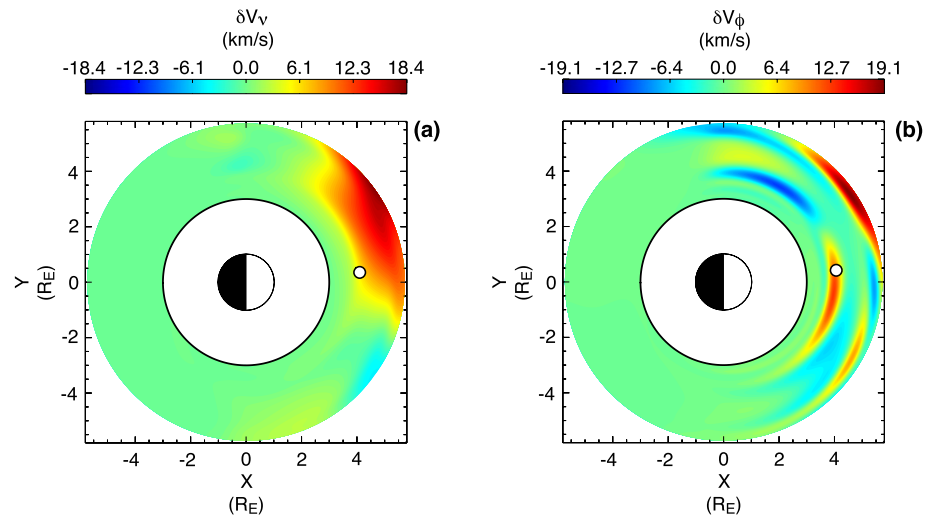
**Figure 11.** (a) Equatorial plane views of $\delta V_\nu$ in the inner portion of the simulation domain at time $t = 5.02$ min. The white dot at location $(X, Y) = (4.07, 0.42\ R_E)$ shows where time series (shown later) are taken from. (b) Same as (a) but for $\delta V_\phi$.

observed. In the real magnetosphere, the outer and inner boundary will not be perfect reflectors of fast mode waves, and global fast mode waves may not last as long as in idealized numerical simulations.

## 5.2. Mass Density Structure and Poloidal Components

When the Alfvén velocity varies with local time, yet another explanation is possible for the poloidal component. Recently, attention has been paid to the relationship between the local time variation of magnetospheric
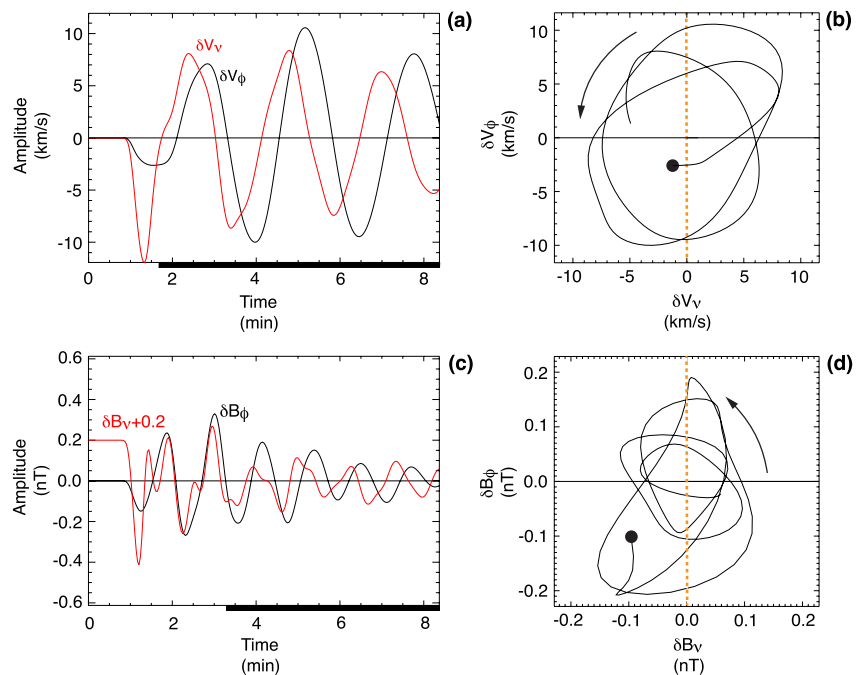


**Figure 12.** (a) Time series of $\delta V_\nu$ (red) and $\delta V_\phi$ (black) from the location of the white dot in Figure 11. (b) Hodogram of the perpendicular velocity components between times 1.7 and 8.4 min, marked by the black horizontal bar at the bottom of panel (a). The black dot indicates the data point at the start of the selected time interval. The orange dotted line indicates the direction for toroidal oscillations. The arrow indicates counterclockwise sense of rotation. (c) Time series from the same location of $\delta B_\nu$ (red) and $\delta B_\phi$ (black). (d) Hodogram of the perpendicular magnetic field components between times 3.35 and 8.4 min, marked by the black horizontal bar at the bottom of panel (c).

mass density and the local time dependence of the physical properties of MHD waves. For example, the larger amplitude of high-latitude ($L > 6$) Pc5 waves on the dawn side than on the dusk side, found in statistical studies (Baker, 2003; Nosé et al., 1995; Takahashi et al., 2015), was attributed to the local time dependence of the coupling efficiency between fast mode waves and Alfvén waves (Takahashi et al., 2016). In a simulation study, Degeling et al. (2018) illustrated how a magnetospheric plasma plume alters the spatial distribution of the amplitude and polarization of externally driven fast mode waves and FLRs. Related numerical studies emphasized that one needs to be careful in distinguishing between toroidal and poloidal waves when the magnetospheric mass density varies with local time (Elsden et al., 2022; Wright & Elsden, 2020; Wright et al., 2018).

With an azimuthally structured Alfvén velocity distribution, such as those associated with a drainage plume, a surface of constant Alfvén frequency is no longer a simple circle. Instead, the surface can be highly distorted with a nearly radial orientation in extreme cases, e.g., at the interface of a plume and the plasmatrough. Because the polarization axis of Alfvén waves excited by FLR tends to be tangential to the surface of constant Alfvén frequency (Wright & Elsden, 2020), we can expect a strong poloidal component in the region of longitudinally localized mass density structures.

The presence of the fast mode appears to be essential to the circular polarization observed by THEMIS-A and RBSP-B (Figure 6) regardless of the local time variation of mass density. A simulation study by Elsden and Wright (2022) incorporating a plume structure demonstrated that polarization in the $\nu - \phi$ plain is circular when the fast mode is coupled to toroidal FLR (see their Figure 3b), just like the polarization obtained in the simulation of the present study (Figure 12). Elsden and Wright (2022) also showed that a plume structure leads to FLRs consisting of radial and azimuthal wave fields but that the polarization is still linear. With our spacecraft observations made in the prenoon sector where drainage plumes are uncommon, our preferred interpretation of the coexisting poloidal and toroidal components is coupling between fast mode waves and toroidal FLRs.

The effect of the drainage plume on ULF waves will be an important subject of future data analysis, e.g., in relation to electron flux oscillations termed boomerang stripes (Zhao et al., 2021). The oscillations appear to be initiated in the postnoon sector and to acquire their characteristic pitch angle versus time pattern as the particle drift azimuthally with pitch angle dependent velocities. ULF waves with a strong poloidal component and localized in the postnoon sector, possibly associated with a drainage plume, may provide an initial perturbation to the electrons.

## 6. Conclusions

We have examined magnetospheric ULF waves observed on the dayside by multiple spacecraft immediately after the impact of an IP shock on 27 February 2014. Some of the waves are noted for their strong poloidal components, unlike shock-induced standing Alfvén waves reported in previous studies. We have run a numerical simulation to understand the spacecraft observations.

The spacecraft data revealed the following properties of the waves:

1. Transverse oscillations accompanying a strong poloidal component were detected by the RBSP-A, RBSP-B, and THEMIS-E spacecraft, which were located in the dayside plasmasphere.
2. The frequencies of the oscillations depend on $L$, as expected for standing Alfvén waves.
3. The two RBSP spacecraft observed little phase delay, eliminating the possibility of internal excitation of high-$m$ waves.

We have obtained the following results from the simulation:

1. Sinusoidal oscillations with mixed poloidal and toroidal components were excited, similar to the spacecraft observations.
2. The poloidal oscillations are attributed to radially standing fast mode waves.
3. The toroidal oscillations are attributed to toroidal standing Alfvén waves resulting from FLRs driven by the fast mode waves.
4. The relative amplitude and phase of the poloidal and toroidal components strongly depend on the radial distance because these two modes have different radial structures.

## Data Availability Statement

The data used in this study are publicly available from the following sources: NASA Goddard Space Flight Center (GSFC) Space Physics Data Facility Coordinated Data Analysis Web (https://cdaweb.gsfc.nasa.gov/index.html) for RBSP data; Space Sciences Laboratory, University of California, Berkeley (http://themis.ssl.berkeley.edu/overview_data.shtml) for THEMIS data; NASA/GSFC Space Physics Data Facility OMNIWeb Plus (https://omniweb.gsfc.nasa.gov/) for solar wind OMNI data; Zenodo archive (Takahashi & Vellante, 2023, https://doi.org/10.5281/zenodo.7838543) for EMMA data; and GFZ German Research Centre for Geosciences (Matzka et al., 2021, https://kp.gfz-potsdam.de/en) for geomagnetic Kp index. Data used to produce the simulation plots are publicly available (Elsden, 2023, https://doi.org/10.6084/m9.figshare.22560115.v1).

## References

Alken, P., Thébault, E., Beggan, C. D., Amit, H., Aubert, J., Baerenzung, J., et al. (2021). International Geomagnetic Reference Field: The thirteenth generation. *Earth Planets and Space*, *73*(1), 49. https://doi.org/10.1186/s40623-020-01288-x

Arthur, C. W., & McPherron, R. L. (1981). The statistical character of Pc 4 magnetic pulsations at synchronous orbit. *Journal of Geophysical Research*, *86*(A3), 1325. https://doi.org/10.1029/JA086iA03p01325

Auster, H. U., Glassmeier, K. H., Magnes, W., Aydogar, O., Baumjohann, W., Constantinescu, D., et al. (2008). The THEMIS fluxgate magnetometer. *Space Science Reviews*, *141*(1–4), 235–264. https://doi.org/10.1007/s11214-008-9365-9

Baker, G. J. (2003). A comprehensive survey of auroral latitude Pc5 pulsation characteristics. *Journal of Geophysical Research*, *108*(A10), 1384. https://doi.org/10.1029/2002JA009801

Baumjohann, W., Junginger, H., Haerendel, G., & Bauer, O. H. (1984). Resonant Alfvén waves excited by a sudden impulse. *Journal of Geophysical Research*, *89*(A5), 2765–2769. https://doi.org/10.1029/JA089iA05p02765

Bonnell, J. W., Mozer, F. S., Delory, G. T., Hull, A. J., Ergun, R. E., Cully, C. M., et al. (2008). The Electric Field Instrument (EFI) for THEMIS. *Space Science Reviews*, *141*(1–4), 303–341. https://doi.org/10.1007/s11214-008-9469-2

Cahill, L. J., Lin, N. G., Waite, J. H., Engebretson, M. J., & Sugiura, M. (1990). Toroidal standing waves excited by a storm sudden commencement: DE 1 observations. *Journal of Geophysical Research*, *95*(A6), 7857. https://doi.org/10.1029/JA095iA06p07857

Chen, L., & Hasegawa, A. (1974). A theory of long-period magnetic pulsations: 1. Steady state excitation of field line resonance. *Journal of Geophysical Research*, *79*(7), 1024–1032. https://doi.org/10.1029/JA079i007p01024

Degeling, A. W., Rae, I. J., Watt, C. E. J., Shi, Q. Q., Rankin, R., & Zong, Q. G. (2018). Control of ULF wave accessibility to the inner magnetosphere by the convection of plasma density. *Journal of Geophysical Research: Space Physics*, *123*, 1086–1099. https://doi.org/10.1002/2017JA024874

Degeling, A. W., Rankin, R., Kabin, K., Rae, I. J., & Fenrich, F. R. (2010). Modeling ULF waves in a compressed dipole magnetic field. *Journal of Geophysical Research*, *115*, A10212. https://doi.org/10.1029/2010JA015410

Elkington, S. R., Hudson, M. K., & Chan, A. A. (1999). Acceleration of relativistic electrons via drift-resonant interaction with toroidal-mode Pc-5 ULF oscillations. *Geophysical Research Letters*, *26*(21), 3273–3276. https://doi.org/10.1029/1999GL003659

Elsden, T. (2023). Data for Takahashi et al., 2023: "Polarization of magnetospheric ULF waves excited by an interplanetary shock on 27 February 2014" Submitted to JGR Space Physics [Dataset]. Figshare. https://doi.org/10.6084/m9.figshare.22560115.v1

Elsden, T., & Wright, A. N. (2019). The effect of fast normal mode structure and magnetopause forcing on FLRs in a 3-D waveguide. *Journal of Geophysical Research: Space Physics*, *124*, 178–196. https://doi.org/10.1029/2018JA026222

Elsden, T., & Wright, A. N. (2022). Polarization properties of 3-D field line resonances. *Journal of Geophysical Research: Space Physics*, *127*, e2021JA030080. https://doi.org/10.1029/2021JA030080

Elsden, T., Yeoman, T. K., Wharton, S. J., Rae, I. J., Sandhu, J. K., Walach, M.-T., et al. (2022). Modeling the varying location of field line resonances during geomagnetic storms. *Journal of Geophysical Research: Space Physics*, *127*, e2021JA029804. https://doi.org/10.1029/2021JA029804

Junginger, H., Geiger, G., Haerendel, G., Melzner, F., Amata, E., & Higel, B. (1984). A statistical study of dayside magnetospheric electric field fluctuations with periods between 150 and 600 s. *Journal of Geophysical Research*, *89*(A7), 5495–5505. https://doi.org/10.1029/JA089iA07p05495

Kaufmann, R. L., & Walker, D. N. (1974). Hydromagnetic-waves excited during an ssc. *Journal of Geophysical Research*, *79*(34), 5187–5195. https://doi.org/10.1029/JA079i034p05187

Kim, K. H. (2002). Magnetospheric responses to sudden and quasiperiodic solar wind variations. *Journal of Geophysical Research*, *107*(A11), 1406. https://doi.org/10.1029/2002JA009342

Kletzing, C. A., Kurth, W. S., Acuna, M., MacDowall, R. J., Torbert, R. B., Averkamp, T., et al. (2013). The Electric and Magnetic Field Instrument Suite and Integrated Science (EMFISIS) on RBSP. *Space Science Reviews*, *179*(1–4), 127–181. https://doi.org/10.1007/s11214-013-9993-6

Korotova, G., Sibeck, D., Thaller, S., Wygant, J., Spence, H., Kletzing, C., et al. (2018). Multisatellite observations of the magnetosphere response to changes in the solar wind and interplanetary magnetic field. *Annales Geophysicae*, *36*(5), 1319–1333. https://doi.org/10.5194/angeo-36-1319-2018

Kurth, W. S., De Pascuale, S., Faden, J. B., Kletzing, C. A., Hospodarsky, G. B., Thaller, S., & Wygant, J. R. (2015). Electron densities inferred from plasma wave spectra obtained by the Waves instrument on Van Allen Probes. *Journal of Geophysical Research: Space Physics*, *120*, 904–914. https://doi.org/10.1002/2014JA020857

Laakso, H., & Schmidt, R. (1989). Pc 4–5 pulsations in the electric field at geostationary orbit (GEOS 2) triggered by sudden storm commencements. *Journal of Geophysical Research*, *94*(A6), 6626–6632. https://doi.org/10.1029/JA094iA06p06626

Lee, D.-H., & Lysak, R. L. (1989). Magnetospheric ULF wave coupling in the dipole model: The impulsive excitation. *Journal of Geophysical Research*, *94*(A12), 17097–17103. https://doi.org/10.1029/JA094iA12p17097

Lichtenberger, J., Clilverd, M. A., Heilig, B., Vellante, M., Manninen, J., Rodger, C. J., et al. (2013). The plasmasphere during a space weather event: First results from the PLASMON project. *Journal of Space Weather and Space Climate*, *3*, A23. https://doi.org/10.1051/swsc/2013045

Mann, I. R., & Wright, A. N. (1995). Finite lifetimes of ideal poloidal Alfvén waves. *Journal of Geophysical Research*, *100*(A12), 23677–23686. https://doi.org/10.1029/95JA02689

Matzka, J., Bronkalla, O., Tornow, K., Elger, K., & Stolle, C. (2021). Geomagnetic Kp index. V. 1.0 [Dataset]. GFZ Data Services. https://doi.org/10.5880/Kp.0001

McFadden, J. P., Carlson, C. W., Larson, D., Bonnell, J., Mozer, F., Angelopoulos, V., et al. (2008). THEMIS ESA first science results and performance issues. *Space Science Reviews*, *141*(1–4), 477–508. https://doi.org/10.1007/s11214-008-9433-1

Nosé, M., Iyemori, T., Sugiura, M., & Slavin, J. A. (1995). A strong dawn/dusk asymmetry in Pc5 pulsation occurrence observed by the DE-1 satellite. *Geophysical Research Letters*, *22*(15), 2053–2056. https://doi.org/10.1029/95GL01794

Oliveira, D. M., Hartinger, M. D., Xu, Z., Zesta, E., Pilipenko, V. A., Giles, B. L., & Silveira, M. V. D. (2020). Interplanetary shock impact angles control magnetospheric ULF wave activity: Wave amplitude, frequency, and power spectra. *Geophysical Research Letters*, *47*, e2020GL090857. https://doi.org/10.1029/2020GL090857

Oliveira, D. M., & Samsonov, A. A. (2018). Geoeffectiveness of interplanetary shocks controlled by impact angles: A review. *Advances in Space Research*, *61*(1), 1–44. https://doi.org/10.1016/j.asr.2017.10.006

Radoski, H. R. (1967). Highly asymmetric MHD resonances: The guided poloidal mode. *Journal of Geophysical Research*, *72*(15), 4026–4027. https://doi.org/10.1029/JZ072i015p04026

Radoski, H. R., & Carovillano, R. L. (1966). Axisymmetric plasmasphere resonances. Toroidal mode. *Physics of Fluids*, *9*(2), 285–291. https://doi.org/10.1063/1.1761671

Shi, Q. Q., Hartinger, M., Angelopoulos, V., Zong, Q. G., Zhou, X. Z., Zhou, X. Y., et al. (2013). THEMIS observations of ULF wave excitation in the nightside plasma sheet during sudden impulse events. *Journal of Geophysical Research: Space Physics*, *118*, 284–298. https://doi.org/10.1029/2012JA017984

Shue, J. H., Chao, J. K., Fu, H. C., Russell, C. T., Song, P., Khurana, K. K., & Singer, H. J. (1997). A new functional form to study the solar wind control of the magnetopause size and shape. *Journal of Geophysical Research*, *102*(A5), 9497–9512. https://doi.org/10.1029/97JA00196

Shue, J. H., Song, P., Russell, C. T., Steinberg, J. T., Chao, J. K., Zastenker, G., et al. (1998). Magnetopause location under extreme solar wind conditions. *Journal of Geophysical Research*, *103*(A8), 17691–17700. https://doi.org/10.1029/98JA01103

Singer, H. J., Matheson, L., Grubb, R., Newman, A., & Bouwer, S. D. (1996). Monitoring space weather with the GOES magnetometers. *Proceedings of the Society of Photo-Optical Instrumentation Engineers*, *2812*, 299–308. https://doi.org/10.1117/12.254077

Southwood, D. J. (1974). Some features of field line resonances in the magnetosphere. *Planetary and Space Science*, *22*(3), 483–491. https://doi.org/10.1016/0032-0633(74)90078-6

Southwood, D. J. (1976). A general approach to low-frequency instability in the ring current plasma. *Journal of Geophysical Research*, *81*(19), 3340–3348. https://doi.org/10.1029/JA081i019p03340

Takahashi, K., Claudepierre, S. G., Rankin, R., Mann, I. R., & Smith, C. W. (2018). Van Allen Probes observation of a fundamental poloidal standing Alfvén wave event related to giant pulsations. *Journal of Geophysical Research: Space Physics*, *123*, 4574–4593. https://doi.org/10.1029/2017JA025139

Takahashi, K., & Denton, R. E. (2021). Nodal structure of toroidal standing Alfvén waves and its implication for field line mass density distribution. *Journal of Geophysical Research: Space Physics*, *126*, e2020JA028981. https://doi.org/10.1029/2020JA028981

Takahashi, K., Hartinger, M. D., Angelopoulos, V., & Glassmeier, K.-H. (2015). A statistical study of fundamental toroidal mode standing Alfvén waves using THEMIS ion bulk velocity data. *Journal of Geophysical Research: Space Physics*, *120*, 6474–6495. https://doi.org/10.1002/2015JA021207

Takahashi, K., Lee, D.-H., Merkin, V. G., Lyon, J. G., & Hartinger, M. D. (2016). On the origin of the dawn-dusk asymmetry of toroidal Pc5 waves. *Journal of Geophysical Research: Space Physics*, *121*, 9632–9650. https://doi.org/10.1002/2016JA023009

Takahashi, K., Lysak, R., & Vellante, M. (2022). Statistical analysis of Pi2 pulsations observed by Van Allen Probes. *Journal of Geophysical Research: Space Physics*, *127*, e2022JA030674. https://doi.org/10.1029/2022JA030674

Takahashi, K., Ohtani, S.-I., & Anderson, B. J. (1995). Statistical analysis of Pi 2 pulsations observed by the AMPTE CCE spacecraft in the inner magnetosphere. *Journal of Geophysical Research*, *100*(A11), 21929–21941. https://doi.org/10.1029/95JA01849

Takahashi, K., Sibeck, D. G., Newell, P. T., & Spence, H. E. (1991). ULF waves in the low-latitude boundary-layer and their relationship to magnetospheric pulsations. A multisatellite observation. *Journal of Geophysical Research*, *96*(A6), 9503–9519. https://doi.org/10.1029/91JA00612

Takahashi, K., & Vellante, M. (2023). EMMA_DATA_2014-02-27 [Dataset]. Zenodo. https://doi.org/10.5281/zenodo.7838543

Tsyganenko, N. A. (1989). A magnetospheric magnetic field model with a warped tail current sheet. *Planetary and Space Science*, *37*(1), 5–20. https://doi.org/10.1016/0032-0633(89)90066-4

Ukhorskiy, A. Y., Takahashi, K., Anderson, B. J., & Korth, H. (2005). Impact of toroidal ULF waves on the outer radiation belt electrons. *Journal of Geophysical Research*, *110*, A10202. https://doi.org/10.1029/2005JA011017

Wang, B., Nishimura, Y., Zhang, H., Shen, X.-C., Lyons, L., Angelopoulos, V., et al. (2019). The 2-D structure of foreshock-driven field line resonances observed by THEMIS satellite and ground-based imager conjunctions. *Journal of Geophysical Research: Space Physics*, *124*, 6792–6811. https://doi.org/10.1029/2019JA026668

Waters, C. L., Menk, F. W., & Fraser, B. J. (1991). The resonance structure of low latitude Pc3 geomagnetic pulsations. *Geophysical Research Letters*, *18*(12), 2293–2296. https://doi.org/10.1029/91GL02550

Wright, A. N. (1994). Dispersion and wave coupling in inhomogeneous MHD waveguides. *Journal of Geophysical Research*, *99*(A1), 159–167. https://doi.org/10.1029/93JA02206

Wright, A. N., & Elsden, T. (2020). Simulations of MHD wave propagation and coupling in a 3-D magnetosphere. *Journal of Geophysical Research: Space Physics*, *125*, e2019JA027589. https://doi.org/10.1029/2019JA027589

Wright, A. N., Elsden, T., & Takahashi, K. (2018). Modeling the dawn/dusk asymmetry of field line resonances. *Journal of Geophysical Research: Space Physics*, *123*, 6443–6456. https://doi.org/10.1029/2018JA025638

Wygant, J., Bonnell, J. W., Goetz, K., Ergun, R. E., Mozer, F. S., Bale, S. D., et al. (2013). The electric field and waves instruments on the radiation belt storm probes mission. *Space Science Reviews*, *179*(1–4), 183–220. https://doi.org/10.1007/s11214-013-0013-7

Wygant, J., Mozer, F., Temerin, M., Blake, J., Maynard, N., Singer, H., & Smiddy, M. (1994). Large-amplitude electric and magnetic field signatures in the inner magnetosphere during injection of 15 MeV electron drift echoes. *Geophysical Research Letters*, *21*(16), 1739–1742. https://doi.org/10.1029/94GL00375

Zhao, X. X., Hao, Y. X., Zong, Q.-G., Zhou, X.-Z., Yue, C., Chen, X. R., et al. (2021). Origin of electron boomerang stripes: Statistical study. *Geophysical Research Letters*, *48*, e2021GL093377. https://doi.org/10.1029/2021GL093377